2020 IEEE/RSJ International Conference on Intelligent Robots and Systems (IROS)
October 25-29, 2020, Las Vegas, NV, USA (Virtual)

Proprioceptive Sensor Fusion for Quadruped Robot State Estimation

Geoff Fink and Claudio Semini

Abstract— **Estimation of a quadruped's state is fundamentally important to its operation. In this paper we develop a low-level state estimator for quadrupedal robots that includes attitude, odometry, ground reaction forces, and contact detection. The state estimator is divided into three parts. First, a nonlinear observer estimates attitude by fusing inertial measurements. The attitude estimator is globally exponentially stable and is able to initialize with large errors in the initial state estimates whereas a state-of-the-art EKF would diverge. This is practical for situations when the robot has fallen over and needs to start from its side. Second, leg odometry is calculated with encoders, force sensors, and torque sensors in the robot's joints. Lastly, the leg odometry and inertial measurements are fused to obtain linear position and velocity. We experimentally validate the state estimator using a novel dataset from the HyQ robot. For the entirety of the experiment the estimated attitude matched the ground truth data and had a root mean square error (RMSE) of [2 1 5] deg, the velocity estimates has a RMSE of [0.11 0.15 0.04] m/s, and the position estimates, which are unobservable, drifted on average [2 1 8] mm/s.**

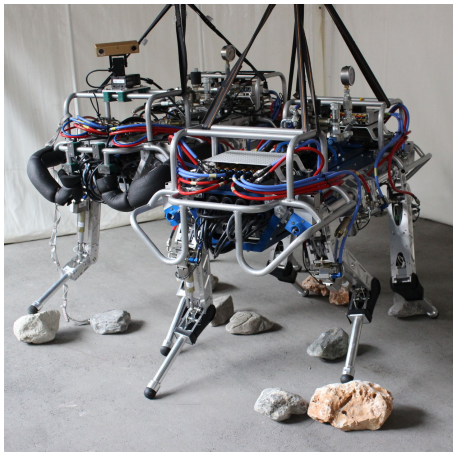

Fig. 1. A photo of two HyQ quadruped robots.

I. Introduction

The development of quadruped robotic platforms is an active area of research in both the public and private sectors [1]–[4]. The higher degrees of freedom provided by legs compared to wheels or tracks allow legged robots to navigate uneven and rough terrain. They are both more mobile and more versatile. However, with the increased mechanical complexity comes an increased difficulty in state estimation and control.

Much of the current literature on state estimation for mobile robotics has been focused on exteroceptive sensors for simultaneous localization and mapping (SLAM) [5], [6], visual odometry [7], [8], visual SLAM [9], and visual-inertial SLAM [10]–[12]. The goal of these works is to provide a non-drifting pose for robot navigation at the task level. However, the main drawbacks of these approaches are the frequencies and delays in many of the sensors used, e.g., cameras and lidars. Furthermore, because they are often designed to be generic, they do not exploit any quadruped model or other sensors commonly found on quadrupeds (i.e., force and torque sensors).

There is also a less numerous, but growing body of literature for state estimation of legged robots at the task level. In [13], [14] the authors proposed an extended Kalman filter (EKF)-based sensor fusion algorithm combining inertial measurements, leg odometry, stereo vision, and lidar. In [15] the authors proposed an EKF-based sensor fusion algorithm combining inertial measurements, leg odometry, stereo vision, and GPS. In [16] the authors proposed an indirect feedback information filter-based algorithm that fuses IMU, leg odometry, and stereo vision. Similar to the SLAM literature these works suffer from the slow update rates of the aiding sensors, such as lidars and cameras.

Lastly, lower level state estimation using only proprioceptive sensors has also been worked on. In [17] the authors proposed a particle filtering-based sensor fusion algorithm, but rely on the terrain being known a priori. In [18] and [19] the authors proposed an observability constrained EKF-based and an unscented Kalman filter (KF)-based algorithm, respectively. However, these works have no stability guarantees and suffer from linearization errors. The most similar work to this work is [2] and [20]. In [20] the author propose simple state estimators for the pose of a humanoid robot. It also proposes decoupling the pose estimation into two cascaded estimators, but does not include a globally exponentially stable (GES) attitude observer. Next, in [2] the authors expanded upon [20] and use a nonlinear observer (NLO) from [21]. However, in the paper few details are given about state estimation as the paper is concentrated on design and control of the robot.

The main contributions of this paper are the proposed low-level state estimator and its experimental validation. We term the state estimator low-level to match our low-level whole-body control that uses velocity commands as inputs. The control requires high-frequency smooth attitude and velocity estimates. It is not used at a task level for robot navigation where non-drifting pose and yaw measurements are

*This research is funded in part by the Italian National Institute for Insurance against Accidents at Work (INAIL). Additionally, the authors would like to thank LORD MicroStrain for providing the 3DM-GX5-15.

The authors are with the Dynamic Legged Systems (DLS) Lab, Istituto Italiano di Tecnologia (IIT), Via Morego 30, 16163, Genova, Italy. E-mail: {geoff.fink,claudio.semini}@iit.it

necessary. This paper builds upon the novel proprioceptive sensor dataset collected on board the hydraulically actuated quadruped HyQ that was presented in a recent conference [22]. The observer design is inspired by [23] and [21]. When compared to previous work [14], the proposed state estimator has a guaranteed stability of its error dynamics and runs at a higher frequency. The attitude observer is GES and the estimated linear velocity are uniformly bounded. Global stability for attitude estimators is practical for situations when the robot has fallen over and needs to start from its side. The higher frequency and bounded velocity estimates decrease pose drift. This is important because, as pointed out in [24], the pose drift in between the high frequency proprioceptive updates and the low frequency exteroceptive updates affected the feed-forward torques and thus the overall execution of a locomotion trajectory for a quadruped robot.

II. Modelling

In this paper we base our model on the hydraulically actuated quadruped HyQ [1] as seen in Fig. 1 and 2. However, the observers are general and can be applied to any legged robot. We consider a floating base robot with four feet and three degrees of freedom (DoFs) per leg. The four legs are labelled left front (LF), right front (RF), left hind (LH), and right hind (RH). Each leg has three actuated joints: hip abduction/adduction (HAA), Hip flexion/extension (HFE), and knee flexion/extension (KFE).

$$\ell \in \mathbb{L} = \{\text{LF}, \text{RF}, \text{LH}, \text{RH}\}$$
$$j \in \mathbb{J} = \{\text{HAA}, \text{HFE}, \text{KFE}\}$$
$$i \in \mathbb{I} = \mathbb{L} \times \mathbb{J}$$

A. Kinematics and Dynamics

Assuming that all of the external forces are exerted on the feet, the dynamics of the robot is

$$M(\bar{x})\ddot{\bar{x}} + h(\bar{x}, \dot{\bar{x}}) = \bar{\tau} \tag{1}$$

where $\bar{x} = \begin{bmatrix} x^T & \eta^T & q^T \end{bmatrix}^T \in \mathbb{R}^{18}$, $x \in \mathbb{R}^3$ is the position of the base, $\eta \in \mathbb{R}^3$ is the attitude of the base, $q \in \mathbb{R}^{12}$ is the vector of joint angles of the robot, $M \in \mathbb{R}^{18\times 18}$ is the joint-space inertia matrix, h is the vector of Coriolis, centrifugal and gravity forces, $\bar{\tau} = (\begin{bmatrix} 0 & \tau^T \end{bmatrix}^T - JF) \in \mathbb{R}^{18}$, $\tau \in \mathbb{R}^{12}$ is the vector of actuated joint torques, $J \in \mathbb{R}^{18\times 12}$ is the floating base Jacobian, and $F \in \mathbb{R}^{12}$ is the vector of external forces.

To further develop the model, we introduce the following frames of reference: the body frame $\mathcal{B}$ which is located at the geometric centre of the trunk, the navigation frame $\mathcal{N}$ which is assumed inertial, and the IMU sensor frame $\mathcal{S}$ which is located at the origin of the accelerometer of the IMU that is mounted onto the trunk of the robot. Additionally, every joint $i \in \mathbb{I}$ has a frame $\mathcal{J}_i$ located at its centre of rotation. The pose of each joint frame $\mathcal{J}_i$ (i.e., the forward kinematics) is assumed to be exactly known. The basis of the body frame are orientated forward, left, and up. We denote the reference frame of a variable using a right superscript, i.e., x^b, x^n, and x^s denote x in $\mathcal{B}$, $\mathcal{N}$, and $\mathcal{S}$, respectively.

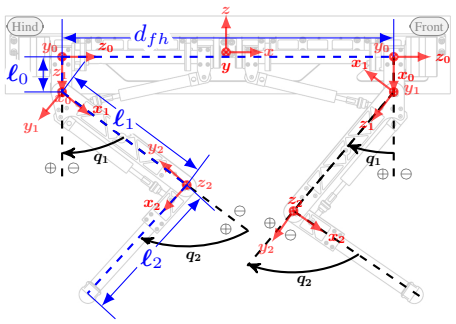

Fig. 2. Diagram of HyQ showing the reference frames for the body and the right legs. The left side is a mirror copy of the right side.

The translational kinematics, translational dynamics, and rotation kinematics in the navigation frame $\mathcal{N}$ are

$$\dot{x}^n = v^n \tag{2a}$$
$$\dot{v}^n = a^n + g^n \tag{2b}$$
$$\dot{R}_b^n = R_b^n S(\omega^b) \tag{2c}$$

where $x^n \in \mathbb{R}^3$, $v^n \in \mathbb{R}^3$, $a^n \in \mathbb{R}^3$ are the position, velocity, and acceleration of the base in $\mathcal{N}$, respectively, $R_b^n \in \text{SO}(3)$ is the rotation matrix from $\mathcal{B}$ to $\mathcal{N}$, and ω^b is the angular velocity of the base in $\mathcal{B}$. The skew symmetric matrix function and its inverse are $S()$ and $\text{vex}()$, respectively, such that $\text{vex}(S(x)) = x$ where $x \in \mathbb{R}^3$.

B. Sensors

The modelling assumes that the quadruped robot is equipped with a six axis IMU (three DoF gyroscope and three DoF accelerometer) on the trunk and that every joint contains a relative encoder, an absolute encoder, and a force or torque sensor. No other sensors such as force sensors in the feet, cameras, nor lidars are required. The accelerometer measures specific force $f_s^s \in \mathbb{R}^3$

$$f_s^s = a^s + g^s \tag{3}$$

where $a^s \in \mathbb{R}^3$ is the acceleration of the body in $\mathcal{S}$ and $g^s \in \mathbb{R}^3$ is the acceleration due to gravity in $\mathcal{S}$. The gyroscope directly measures angular velocity $\omega^s \in \mathbb{R}^3$ in $\mathcal{S}$. The absolute and relative encoders are used to measure the joint position $q_i \in \mathbb{R}$ and joint speed $\dot{q}_i \in \mathbb{R}$, respectively, in $\mathcal{J}_i$. However, due to the speed and accuracy of the relative encoder compared to the absolute encoder, the absolute encoder is only used to measure the initial angle of the joint $q_i(t=0)$ and then all future joint positions are found using the relative encoder. The torque sensors in the HAA joints $i \in \{\mathbb{L} \times \text{HAA}\}$ directly measure torque $\tau_i \in \mathbb{R}^3$. The force sensors in the HFE and KFE joints $i \in \{\mathbb{L} \times \{\text{HFE}, \text{KFE}\}\}$ can be used to calculate τ_i by using the time-varying cylinder lever arm $c_i(q(t)) > 0 \in \mathbb{R}$.

$$\tau_i = \begin{cases} \tau_i & i \in \mathbb{L} \times \{\text{HAA}\} \\ c_i f_i & i \in \mathbb{L} \times \{\text{HFE}, \text{KFE}\} \end{cases} \tag{4}$$

The measured values of the sensors differ from the theoretical values in that they contain a bias and noise.

$$\tilde{x} = x + b_x + n_x \tag{5}$$

where $\tilde{x}$, b_x, and n_x are the measured value, bias, and noise of x, respectively. All of the biases are assumed to be constant or slowly time-varying, and all of the noise variables have zero mean and a Gaussian distribution.

C. Ground Reaction Forces

We solve for the ground reaction forces F_ℓ of each leg $\ell \in \mathbb{L}$ using the actuated part of the dynamics in (1).

$$F_\ell = -\alpha_\ell (J_\ell^T(q_\ell))^{-1}(\tau_\ell - h_\ell(\bar{x}_\ell, \dot{\bar{x}}_\ell)) \tag{6}$$

$F_\ell \in \mathbb{R}^3 \subset F$ is the ground reaction force for ℓ in $\mathcal{B}$, $J_\ell \in \mathbb{R}^{3\times 3} \subset J$ is the foot Jacobian of ℓ, $\tau_\ell \in \mathbb{R}^3 \subset \tau$ is the vector of joint torques of ℓ in $\mathcal{J}_i$, $h_\ell \in \mathbb{R}^3 \subset h$ is the vector of centrifugal, Coriolis, gravity torques of ℓ in $\mathcal{B}$, and $\alpha_\ell \in \{0, 1\}$ selects if the foot is on the ground or not. A threshold of F_ℓ is typically used to calculate α_ℓ.

$$\alpha_\ell = \begin{cases} 1 & ||(J_\ell^T)^{-1}(\tau_\ell - h_\ell)|| > \epsilon \\ 0 & \text{otherwise} \end{cases} \tag{7}$$

where $\epsilon > 0 \in \mathbb{R}$ is the threshold.

D. Leg Odometry

Assuming that there is no slippage, then the contribution of each leg $\ell \in \mathbb{L}$ to the overall velocity of the base is

$$\dot{x}_\ell^b = -\alpha_\ell \left(J_\ell(q_\ell)\dot{q} - \omega^b \times x_\ell^b \right) \tag{8}$$

and the base velocity is

$$\dot{x}^b = \frac{1}{n_s} \sum_\ell^{\mathbb{L}} \dot{x}_\ell^b \tag{9}$$

where $n_s = \sum_\ell^{\mathbb{L}} \alpha_\ell$ is the number of stance legs.

III. State Estimator

The low-level state estimator includes input from three proprioceptive sensors: an IMU, encoders, force sensors, and torque sensors. For reliability and speed no exteroceptive sensors are used. The state estimator consists of three major components: an attitude observer, leg odometry, and a sensor fusion algorithm. An overview of the system can be seen in Fig. 3.

A. Attitude Observers

Typically in the literature an EKF is used for attitude estimation, e.g., [13], [15], [16], [19]. For convenience we provide the equations below. Given the dynamics $\dot{x} = f_x(x, u)$ and $z = h_x(x)$ where $x \in \mathbb{R}^n$ is the state, $u \in \mathbb{R}^p$ is the input, $z \in \mathbb{R}^m$ is the output, and f_x and

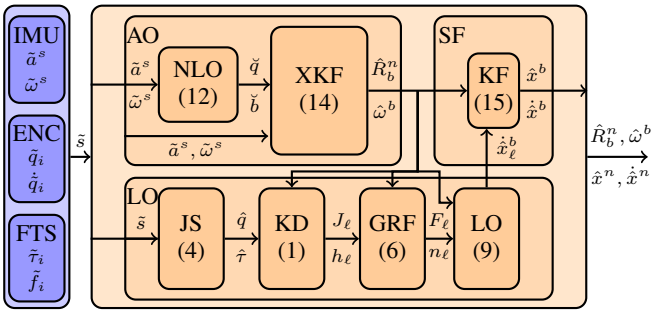

Fig. 3. The low-level state estimator (orange) includes input from three proprioceptive sensors (blue): an IMU, encoders (ENC), and force and torque sensors (FTS); and consists of three major blocks: an attitude observer (AO), leg odometry (LO), and a sensor fusion algorithm (SF). The AO block includes a nonlinear observer (NLO) and and eXogeneous Kalman Filter (XKF). The LO block includes the joint state (JS), the kinematic and dynamic model of the robot (KD), the ground reaction forces model (GRF), and the leg odometry model. Lastly, the SF block includes a Kalman filter (KF). Each block (except the sensor input) contains its corresponding equation number for easy reference.

h_x are differentiable functions of the state and input then the continuous time EKF is

$$\begin{aligned} \dot{\hat{x}} &= f_x + K(z - h_x) \\ \dot{P} &= FP + PF^T - KHP + Q \\ K &= PH^T R^{-1} \end{aligned} \tag{10}$$

where $F = \partial f_x / \partial x|_{\hat{x},u}$, $H = \partial h_x / \partial x|_{\hat{x},u}$, $K \in \mathbb{R}^{n\times m}$ is the Kalman gain, $P \in \mathbb{R}^{n\times n}$ is the covariance matrix, $Q \in \mathbb{R}^{n\times n}$ is the process noise and $R \in \mathbb{R}^{m\times m}$ is the measurement noise covariance.

For attitude estimation we chose to use a quaternion to represent the rotation as it does not contain singularities. Thus, the dynamics is

$$\begin{aligned} \dot{\mathfrak{q}}_b^n &= \frac{1}{2} \begin{bmatrix} 0 & -(\omega^b - b^b)^T \\ (\omega^b - b^b) & -S(\omega^b - b^b) \end{bmatrix} \mathfrak{q}_b^n \\ \dot{b}^b &= 0 \end{aligned} \tag{11}$$

The state, input and output are $x = \begin{bmatrix} \mathfrak{q}^T & b^T \end{bmatrix}^T \in \mathbb{R}^7$, $u = \omega^b \in \mathbb{R}^3$, and $z = R_n^b y^n$, respectively, where y^n are a set of k constant references vectors in $\mathcal{N}$.

$$\begin{aligned} y^b &= \begin{bmatrix} (y_1^b)^T & \cdots & (y_k^b)^T \end{bmatrix}^T \in \mathbb{R}^{3k} \\ y^n &= \begin{bmatrix} (y_1^n)^T & \cdots & (y_k^n)^T \end{bmatrix}^T \in \mathbb{R}^{3k} \end{aligned}$$

Next, we note that instead of using an additive quaternion error function, i.e., $e_\mathfrak{q} = \mathfrak{q}_b^n - \hat{\mathfrak{q}}_b^n$, which can violate the quaternion norm constraint, we use a multiplicative error.

$$e_\mathfrak{q} = (\mathfrak{q}_b^n)^{-1} \otimes \hat{\mathfrak{q}}_b^n$$

where $\otimes$ is quaternion multiplication. For more information the interested reader is referred to [25].

1) Non-linear Observer: Starting in [21] the authors introduced a class of non-linear observers (NLOs) for attitude estimation that make use of symmetry properties of the group structure to have strong convergence properties [26]. There

have been many extensions to these works, in particular we use the observer in [27]. The attitude observer is

$$\dot{\hat{R}}_b^n = \hat{R}_b^n S(\omega^b - \hat{b}^b) + \sigma K_p J(\hat{R}_b^n) \tag{12a}$$

$$\dot{\hat{b}}^b = \text{Proj}\left(\hat{b}^b, -k \,\text{vex}\left(\mathbb{P}\left(\hat{R}_n^b K_p J(\hat{R}_{bs}^n)\right)\right)\right) \tag{12b}$$

where $K_p \in \mathbb{R}^{3\times3}$ is a symmetric positive-definite gain matrix, $k > 0 \in \mathbb{R}$ is a scalar gain, $\sigma \geq 1 \in \mathbb{R}$ is a scaling factor, $\hat{R}_{bs}^n = \text{sat}(\hat{R}_s^n)$, the function $\text{sat}(X)$ saturates every element of X to ±1, Proj is a parameter projection that ensures that $||\hat{b}|| < M_b$, $M_b > 0 \in \mathbb{R}$ is a constant known upper bound on the gyro bias, $\mathbb{P}(X) = \frac{1}{2}(X + X^T)$ for any square matrix X, and J is the stabilizing injection term

$$J(\hat{R}_b^n, t) = \sum_{j=1}^{k} (y_j^n - \hat{R}_b^n y_j^b) y_j^{bT}$$

The observer is GES for all initial conditions assuming there exists $k > 1$ non-collinear vector measurements, i.e.,

$$\left|y_i^n \times y_j^n\right| > 0$$

where $i, j \in \{1, \cdots, k\}$. Furthermore, if there is only one measurement the observer is still GES if the following persistency of excitation (PE) condition holds: If there exist constants $T > 0 \in \mathbb{R}$ and $\gamma > 0 \in \mathbb{R}$ such that, for all $t \geq 0$

$$\int_t^{t+T} y_1^n(\tau) y_1^n(\tau)^T \, d\tau \geq \gamma I \tag{13}$$

holds then y_1^n is PE. See [27] for proof.

2) eXogeneous Kalman Filter: The eXogeneous Kalman Filter (XKF) [23] is similar to an EKF in that it linearizes a nonlinear model about an estimate of the state and then applies the typical linear time-varying (LTV) KF to the linearized model. If the estimate is close to the true state then the filter is near-optimal. However, if the estimate is not close to the true state the filter can quickly diverge. To overcome this problem the XKF linearizes about a globally stable exogenous signal from a NLO. The cascaded structure maintains the global stability properties from the NLO and the near-optimal properties from the KF. The observer is

$$\dot{\hat{x}} = f_x + F(\hat{x} - \breve{x}) + K\left(z - h_x - H(\hat{x} - \breve{x})\right) \tag{14a}$$

$$\dot{P} = FP + PF^T - KHP + Q \tag{14b}$$

$$K = PH^T R^{-1} \tag{14c}$$

where $F = \partial f_x / \partial x|_{\breve{x},u}$, $H = \partial h_x / \partial x|_{\breve{x},u}$, $\breve{x} \in \mathbb{R}^n$ is the bounded estimate of x from the globally stable NLO. See [23] for the stability proof.

B. Sensor Fusion

Lastly, the inertial measurements (3) are fused with the leg odometry (9). The main advantage of decoupling the attitude from the position and linear velocity is that the resulting dynamics is LTV, and thus has guaranteed stability properties. i.e., the filter will not diverge in finite time.

We use a LTV KF with the dynamics (2), the accelerometer (3), and leg odometry (9).

$$\begin{aligned} \dot{\hat{\underline{x}}} &= f_{\underline{x}} + \underline{K}(\underline{z} - h_{\underline{x}}) \\ \dot{\underline{P}} &= \underline{F}\underline{P} + \underline{P}\underline{F}^T - \underline{K}\underline{H}\underline{P} + \underline{Q} \\ \underline{K} &= \underline{P}\underline{H}^T \underline{R}^{-1} \end{aligned} \tag{15}$$

where the state $\underline{x} = \begin{bmatrix} x^{nT} & v^{nT} \end{bmatrix}^T \in \mathbb{R}^6$ is position and velocity of the base, the input $u = (R_b^n f_s^b - g^n) \in \mathbb{R}^3$ is the acceleration of the base, the measurement $z = R_b^n x_\ell^b \in \mathbb{R}^3$ is the leg odometry, $\underline{K} \in \mathbb{R}^{6\times3}$ is the Kalman gain, $P \in \mathbb{R}^{6\times6}$ is the covariance matrix, $Q \in \mathbb{R}^{6\times6}$ is the process noise and $R \in \mathbb{R}^{3\times3}$ is the measurement noise covariance, and

$$f_{\underline{x}} = \begin{bmatrix} v^n \\ u \end{bmatrix} \quad \underline{F} = \begin{bmatrix} 0_3 & I_3 \\ 0_3 & 0_3 \end{bmatrix} \quad \underline{H} = \begin{bmatrix} 0_3 & I_3 \end{bmatrix}$$

and I_3 and 0_3 are the 3×3 identity matrix and matrix of all zeros, respectively.

IV. Experimental Results

The experimental platform used to evaluate the proposed state estimator is the robot HyQ. A photo of HyQ is shown in Fig. 1 and a model in Fig. 2. HyQ weighs approximately 90 kg depending on its current sensor suite and has twelve torque-controlled joints powered by hydraulic actuators. The hydraulic actuators allow the robot to perform powerful dynamic motions. Detailed mechanical specifications for HyQ are in [1] and [28]. Using this platform a proprioceptive sensor dataset was published in [29]. In the "Trot in Lab" dataset HyQ was manually controlled to trot around the laboratory. Trotting is difficult for state estimators because of the dynamic motions, vibrations, and potential foot slippage. The sequence includes: forward and backwards motion, side-to-side motion, zig-zags, yaw motion, and a mix of linear and yaw motion. All of the sensors were recorded at 1000 Hz. Additionally, a motion capture system (MCS) recorded the ground truth data with millimetre accuracy at 250 Hz. Further details on the dataset including the raw data from this experiment is described in and can be found in [29].

The raw data from the experiment is plotted in Fig. 4 – 7. Each figure contains a plot with the data for the entire experiment $0 \leq t \leq 300$ s and a plot zoomed in at two seconds of the experiment $30 \leq t \leq 32$ s. Fig. 4 shows the specific force (3) measured by the IMU after is has been rotated from the sensor frame $\mathcal{S}$ to the body frame $\mathcal{B}$. The acceleration due to gravity can been seen in the z-axis, and we can see that there is more noise in the z-axis caused by vibrations after the foot impacts with the ground while trotting. Fig. 5 shows the angular velocity in $\mathcal{B}$. Similarly, we can see the trunk of the robot is rotating slightly from side-to-side and back-and-forth as the robot trots. There is relatively minor yaw rotation in a regular trot unless, of course, the robot is commanded to turn. Fig. 6 shows the joint position of the six joints in the front legs. The hind legs have been omitted due to space constraints. As is expected there is minor motion in the HAAs; and the HFE and KFE can be seen following a trotting gait. Fig. 7 shows the measured

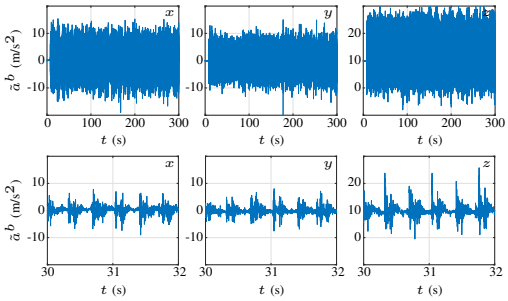

Fig. 4. The specific force $\tilde{a}^b$ in the body frame $\mathcal{B}$ measured on board HyQ during a trotting experiment. The top row shows the full experiment ($0\text{ s} \leq t \leq 300\text{ s}$) and the bottom row is zoomed in ($30\text{ s} \leq t \leq 32\text{ s}$).

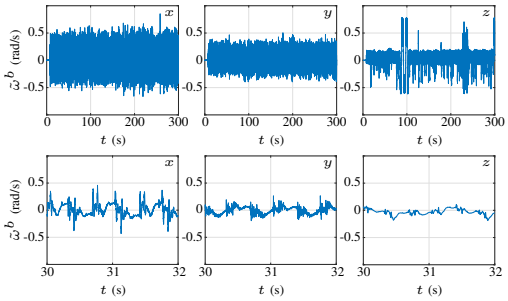

Fig. 5. The angular velocity $\tilde{\omega}^b$ in body frame $\mathcal{B}$ measured on board HyQ during a trotting experiment. The top row shows the full experiment ($0\text{ s} \leq t \leq 300\text{ s}$) and the bottom row is zoomed in ($30\text{ s} \leq t \leq 32\text{ s}$).

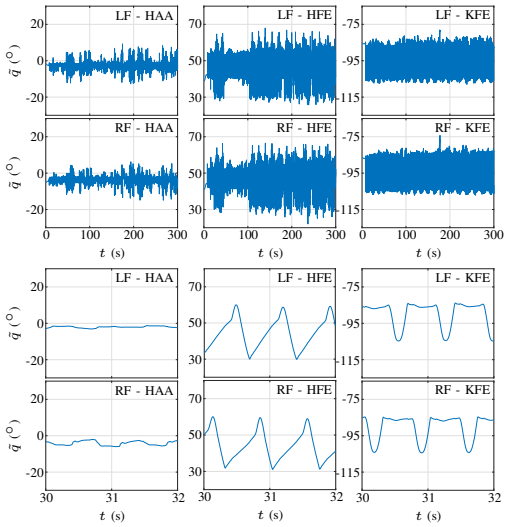

Fig. 6. The joint position $\tilde{q}$ measured in the joint frame $\mathcal{J}_i$ on board HyQ during a trotting experiment. The top two rows shows the full experiment ($0\text{ s} \leq t \leq 300\text{ s}$) and the bottom two rows are zoomed in ($30\text{ s} \leq t \leq 32\text{ s}$).

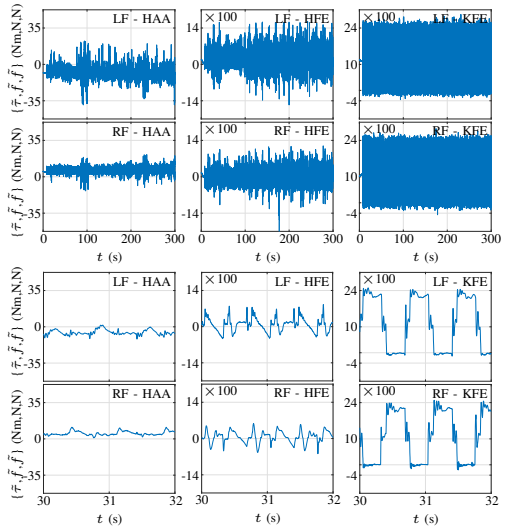

Fig. 7. The measured force $\tilde{f}_i$, $i \in \{\{HFE, KFE\} \times \mathbb{L}\}$ and torque $\tilde{\tau}_i$, $i \in \{HAA \times \mathbb{L}\}$ in the joint frame $\mathcal{J}_i$ measured on board HyQ during a trotting experiment. The top two rows shows the full experiment ($0\text{ s} \leq t \leq 300\text{ s}$) and the bottom two rows are zoomed in ($30\text{ s} \leq t \leq 32\text{ s}$).

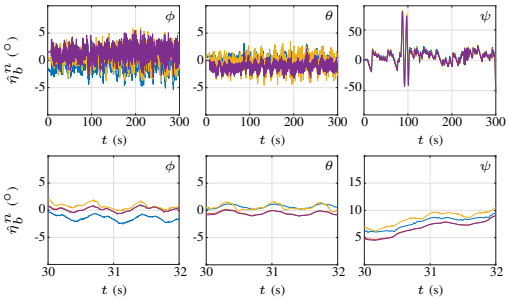

Fig. 8. The estimated attitude $\hat{\eta}_b^n$ of HyQ during a trotting experiment using an EKF (orange), a NLO (yellow), and an XKF (purple) versus the motion capture attitude (blue). All of the observers demonstrate similar steady state behaviour when the initial conditions were chosen close to the actual values. The top row shows the full experiment ($0\text{ s} \leq t \leq 300\text{ s}$) and the bottom row is zoomed in ($30\text{ s} \leq t \leq 32\text{ s}$).

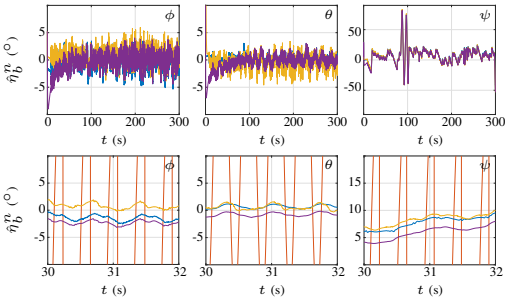

Fig. 9. The estimated attitude $\hat{\eta}_b^n$ of HyQ during a trotting experiment using an EKF (orange), a NLO (yellow), and an XKF (purple) versus the motion capture attitude (blue). When there is a large initial condition (the robot starting on its side) the EKF diverges whereas the NLO and XKF converge. The top row shows the full experiment ($0\text{ s} \leq t \leq 300\text{ s}$) and the bottom row is zoomed in ($30\text{ s} \leq t \leq 32\text{ s}$).

forces and torques in the joints. The trotting gait can easily be seen particularly in the KFE.

The output from the attitude observers in the experiment is plotted in Fig. 8 – 11. We compare our observer against the industry standard EKF. In the figures the motion capture ground truth is plotted in blue, the EKF is plotted in orange, the NLO is plotted in yellow, and the XKF is plotted in purple. A typical experiment can be seen in Fig. 8. Both the robot and the observers are initialized in a horizontal position. In the figure all of the observer have similar steady state performance and are all within a couple of degrees of the motion capture ground truth. The root mean square error (RMSE) was $\begin{bmatrix}2 & 1 & 5\end{bmatrix}^T$ °. However, in Fig. 9 the observers have been initialized with a large initial error and the global stability of the NLO and XKF become immediately evident. The EKF diverges and is not able to recover. This experiment is meant to demonstrate what would happen if the robot were to fall on its side and it has to re-initialize it state.

Fig. 10 shows the estimation of the ground reaction forces per leg in the z-direction of the $\mathcal{B}$ (6). The foot loading, unloading, and stance phases along with vibration, noise, and slippage can be seen in the figure. The shaded region represents when the foot is in contact with the ground (7). From the data we can also verify that during the trot each of the two legs is supporting approximately half the weight of the robot. After we have calculated when the feet are in contact with the ground we can calculate the leg odometry. The raw leg odometry is plotted in Fig. 11 in green. The bottom row of the figure also is a good example of what forward velocity of a trot gait looks like.

The output from the sensor fusion in the experiment is plotted in Fig. 11 – 12. In the figures the raw leg odometry is plotted in green, the motion capture ground truth is plotted in blue, and our proposed sensor fusion (KF) is plotted in purple. The figure shows good performance of both the velocity and position estimates. The estimated velocity has a RMSE of $\begin{bmatrix}0.11 & 0.15 & 0.04\end{bmatrix}^T$ m/s, and the estimated position drifted on average $\begin{bmatrix}2 & 1 & 8\end{bmatrix}^T$ mm/s.

A. Discussion

It is interesting to note that the dataset contains two different IMU's: the KVH-1775 and the 3DM-GX5-15. While the noise characteristics of the IMU's are very different, very little difference in performance was seen after sensor fusion. Due to the lack of differences in the state estimates using the two IMU's the plots have been omitted for space. The gyroscope measurements of the KVH are supposed to have zero bias, however the observers were left free to estimate the bias. The observers verified the zero bias. The estimated biases for the experiment were $b^b = \begin{bmatrix}0.0 & 0.0 & 0.1\end{bmatrix}^T \times 10^{-3}$ rad/s and $b^b = \begin{bmatrix}0.0 & 4.3 & 1.7\end{bmatrix}^T \times 10^{-3}$ rad/s for the KVH and 3DM, respectively.

The calculations for the ground reaction forces involved the calculation of the vector of Coriolis, centrifugal, and gravity forces $h(\bar{x}, \dot{\bar{x}})$. As an initial pass it was assumed that the accelerations $\ddot{x}^b = \dot{\omega}^b = 0$. The noise in the variables is

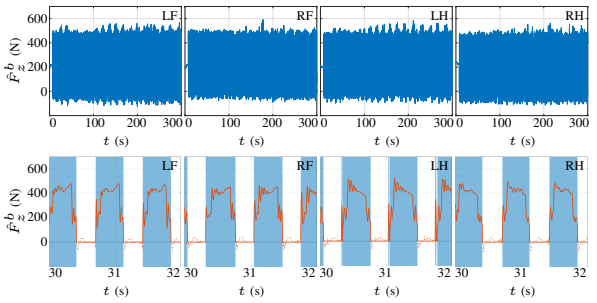

Fig. 10. The z component of the estimated ground reaction forces $\hat{F}_z^b$ in the body frame $\mathcal{B}$ of HyQ during a trotting experiment. The highlighted regions show when the given foot is in stance. The top row shows the full experiment (0 s $\leq t \leq$ 300 s) and the bottom row is zoomed in (30 s $\leq t \leq$ 32 s).

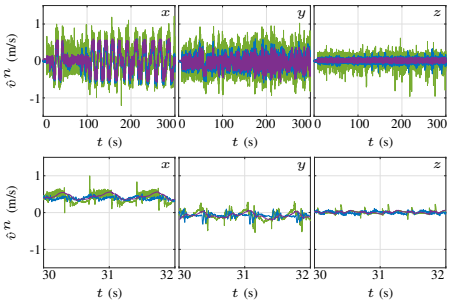

Fig. 11. The estimated trunk velocity $\hat{v}^n$ in the navigation frame $\mathcal{N}$ of HyQ during a trotting experiment using sensor fusion (purple) versus the raw leg odometry (green), and the motion capture system (blue). The top row shows the full experiment (0 s $\leq t \leq$ 300 s) and the bottom row is zoomed in (30 s $\leq t \leq$ 32 s).

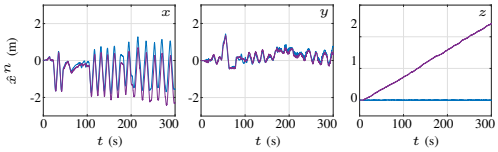

Fig. 12. The estimated trunk position $\hat{x}^n$ in the navigation frame $\mathcal{N}$ of HyQ during a trotting experiment using sensor fusion (purple) versus the motion capture system (blue).

typically much larger then their effect, but they might make more of an impact in highly dynamic manoeuvres.

The differences in the observers and the ground truth of less then two degrees should be ignored as it is within the error of measurement of the ground truth. Furthermore the tolerance of the mechanical parts allows for the IMU's and motion capture markers to be different by a couple of degrees. For higher accuracy measurements a different test platform would have to be developed. However, this level of accuracy is not necessary nor useful for current quadruped locomotion strategies. What is important to note is the attitude observer state estimates did not drift for the entirety of the five minute experiment. Longer missions could be useful to measure slower drift.

V. Conclusion

In this paper, we developed a low-level state estimator for quadrupedal robots to estimate pose and velocity of the

base of a quadruped robot using only proprioceptive sensors. For attitude estimation it includes a nonlinear observer that is globally exponentially stable. Leg odometry is calculated using a quadruped model. Lastly, inertial measurements were fused with leg odometry in a KF. The velocity estimates are uniformly bounded. We experimentally validated the state estimator using a novel dataset from the HyQ robot. For the entirety of the dataset the estimated attitude matched the ground truth data and did not drift. The attitude has a root mean square error (RMSE) of $\begin{bmatrix}2 & 1 & 5\end{bmatrix}^T$ °. The attitude estimator is able to initialize with large initial conditions whereas a state-of-the-art EKF would diverge. This is practical for situations when the robot has fallen over and needs to start from its side. The velocity estimates has a RMSE of $\begin{bmatrix}0.11 & 0.15 & 0.04\end{bmatrix}^T$ m/s. The position estimates, which are unobservable, drifted on average $\begin{bmatrix}2 & 1 & 8\end{bmatrix}^T$ mm/s.

Future works include extending the state estimator to include further parameter estimation and intra-sensor calibration. Additionally, further datasets will be recorded to measure the long-term drift of the IMU biases and what effect it may have on the state estimator.

REFERENCES

[1] C. Semini, N. G. Tsagarakis, E. Guglielmino, M. Focchi, F. Cannella, and D. G. Caldwell, "Design of HyQ – a hydraulically and electrically actuated quadruped robot," *Proc. Inst. Mech. Eng. I J. Syst. Control Eng.*, vol. 225, no. 6, pp. 831–849, 2011, DOI:10.1177/0959651811402275.

[2] G. Bledt, M. J. Powell, B. Katz, J. Di Carlo, P. M. Wensing, and S. Kim, "MIT Cheetah 3: Design and control of a robust, dynamic quadruped robot," in *Int. Conf. on Intell. Robots and Syst. (IROS)*, Madrid, Spain, Oct. 2018, pp. 2245–2252, DOI:10.1109/IROS.2018.8593885.

[3] M. Hutter, C. Gehring, D. Jud, A. Lauber, C. D. Bellicoso, V. Tsounis, J. Hwangbo, K. Bodie, P. Fankhauser, M. Bloesch, R. Diethelm, S. Bachmann, A. Melzer, and M. Hoepflinger, "ANYmal - a highly mobile and dynamic quadrupedal robot," in *Int. Conf. on Intell. Robots and Syst. (IROS)*, Daejeon, South Korea, Oct. 2016, pp. 38–44, DOI:10.1109/IROS.2016.7758092.

[4] M. Raibert, K. Blankespoor, G. Nelson, and R. Playter, "Bigdog, the rough-terrain quadruped robot," *IFAC Proceedings Volumes*, vol. 41, no. 2, pp. 10 822–10 825, 2008, DOI:10.3182/20080706-5-KR-1001.01833.

[5] H. Durrant-Whyte and T. Bailey, "Simultaneous localization and mapping: part I," *IEEE Robot. Autom. Mag.*, vol. 13, no. 2, pp. 99–110, Jun. 2006, DOI:10.1109/MRA.2006.1638022.

[6] T. Bailey and H. Durrant-Whyte, "Simultaneous localization and mapping (SLAM): part II," *IEEE Robot. Autom. Mag.*, vol. 13, no. 3, pp. 108–117, Sep. 2006, DOI:10.1109/MRA.2006.1678144.

[7] D. Scaramuzza and F. Fraundorfer, "Visual odometry [tutorial]," *IEEE Robot. Autom. Mag.*, vol. 18, no. 4, pp. 80–92, Dec. 2011, DOI:10.1109/MRA.2011.943233.

[8] F. Fraundorfer and D. Scaramuzza, "Visual odometry : Part II: Matching, robustness, optimization, and applications," *IEEE Robot. Autom. Mag.*, vol. 19, no. 2, pp. 78–90, Jun. 2012, DOI:10.1109/MRA.2012.2182810.

[9] A. J. Davison, I. D. Reid, N. D. Molton, and O. Stasse, "MonoSLAM: Real-time single camera SLAM," *IEEE Trans. Pattern Anal. Mach. Intell*, vol. 29, no. 6, pp. 1052–1067, Jun. 2007, DOI:10.1109/TPAMI.2007.1049.

[10] A. Concha, G. Loianno, V. Kumar, and J. Civera, "Visual-inertial direct SLAM," in *IEEE Int. Conf. Robot. Autom. (ICRA)*, Stockholm, Sweden, May 2016, pp. 1331–1338, DOI:10.1109/ICRA.2016.7487266.

[11] T. Pire, R. Baravalle, A. D'Alessandro, and J. Civera, "Real-time dense map fusion for stereo SLAM," *Robotica*, vol. 36, no. 10, pp. 1510–1526, 2018, DOI:10.1017/S0263574718000528.

[12] J. Engel, J. Sturm, and D. Cremers, "Scale-aware navigation of a low-cost quadrocopter with a monocular camera," *Robot. Auton, Syst.*, vol. 62, no. 11, pp. 1646–1656, 2014, special Issue on Visual Control of Mobile Robots. DOI:10.1016/j.robot.2014.03.012.

[13] S. Nobili, M. Camurri, V. Barasuol, M. Focchi, D. Caldwell, C. Semini, and M. Fallon, "Heterogeneous sensor fusion for accurate state estimation of dynamic legged robots," in *Proc. of Robot.: Sci. and Syst. (RSS)*, Cambridge, Massachusetts, Jul. 2017, pp. 1–9, DOI:10.15607/RSS.2017.XIII.007.

[14] M. Camurri, M. Fallon, S. Bazeille, A. Radulescu, V. Barasuol, D. G. Caldwell, and C. Semini, "Probabilistic contact estimation and impact detection for state estimation of quadruped robots," *IEEE Robot. Autom. Lett.*, vol. 2, no. 2, pp. 1023–1030, Apr. 2017, DOI:10.1109/LRA.2017.2652491.

[15] J. Ma, M. Bajracharya, S. Susca, L. Matthies, and M. Malchano, "Real-time pose estimation of a dynamic quadruped in gps-denied environments for 24-hour operation," *Int. J. of Robotics Res.*, vol. 35, no. 6, pp. 631–653, 2016, DOI:10.1177/0278364915587333.

[16] A. Chilian, H. Hirschmüller, and M. Görner, "Multisensor data fusion for robust pose estimation of a six-legged walking robot," in *Int. Conf. on Intell. Robots and Syst. (IROS)*, San Francisco, CA, Sep. 2011, pp. 2497–2504, DOI:10.1109/IROS.2011.6094484.

[17] S. Chitta, P. Vernaza, R. Geykhman, and D. D. Lee, "Proprioceptive localilzatilon for a quadrupedal robot on known terrain," in *IEEE Int. Conf. Robot. Autom. (ICRA)*, Roma, Italy, Apr. 2007, pp. 4582–4587, DOI:10.1109/ROBOT.2007.364185.

[18] M. Bloesch, M. Hutter, M. Hoepflinger, S. Leutenegger, C. Gehring, C. D. Remy, and R. Siegwart, "State estimation for legged robots - consistent fusion of leg kinematics and IMU," in *Proc. of Robot.: Sci. and Syst. (RSS)*, Sydney, Australia, July 2012, pp. 1–8, DOI:10.15607/RSS.2012.VIII.003.

[19] M. Bloesch, C. Gehring, P. Fankhauser, M. Hutter, M. A. Hoepflinger, and R. Siegwart, "State estimation for legged robots on unstable and slippery terrain," in *Int. Conf. on Intell. Robots and Syst. (IROS)*, Tokyo, Japan, Nov. 2013, pp. 6058–6064, DOI:10.1109/IROS.2013.6697236.

[20] T. Flayols, A. Del Prete, P. Wensing, A. Mifsud, M. Benallegue, and O. Stasse, "Experimental evaluation of simple estimators for humanoid robots," in *IEEE Int. Conf. Humanoid Robots (Humanoids)*, Birmingham, UK, Nov. 2017, pp. 889–895, DOI:10.1109/HUMANOIDS.2017.8246977.

[21] R. Mahony, T. Hamel, and J. Pflimlin, "Nonlinear complementary filters on the special orthogonal group," *IEEE Trans. Autom. Control*, vol. 53, no. 5, pp. 1203–1218, Jun. 2008, DOI:10.1109/TAC.2008.923738.

[22] G. Fink and C. Semini, "The DLS quadruped proprioceptive sensor dataset," in *Int. Conf. Ser. on Climbing and Walking Robots*, Moscow, Russia, Aug. 2020, pp. 1–8.

[23] T. A. Johansen and T. I. Fossen, "The eXogenous Kalman Filter (XKF)," *Int. J. Control*, vol. 90, no. 2, pp. 161–167, 2017, DOI:10.1080/00207179.2016.1172390.

[24] C. Mastalli, I. Havoutis, M. G. Focchi, D. G. Caldwell, and C. G. Semini, "Motion planning for quadrupedal locomotion: coupled planning, terrain mapping and whole-body control," Oct. 2018, preprint. [Online]. Available: https://hal.laas.fr/hal-01673438

[25] F. Markley and J. Crassidis, *Fundamentals of Spacecraft Attitude Determination and Control*, ser. Space Technology Library. New York, New York: Springer, 2014, DOI:10.1007/978-1-4939-0802-8.

[26] R. Mahony, J. Trumpf, and T. Hamel, "Observers for kinematic systems with symmetry," *IFAC Proceedings Volumes*, vol. 46, no. 23, pp. 617–633, 2013, DOI:10.3182/20130904-3-FR-2041.00212.

[27] H. F. Grip, T. I. Fossen, T. A. Johansen, and A. Saberi, "Globally exponentially stable attitude and gyro bias estimation with application to gnss/ins integration," *Automatica*, vol. 51, pp. 158–166, 2015, DOI:10.1016/j.automatica.2014.10.076.

[28] C. Semini, "HyQ - design and development of a hydraulically actuated quadruped robot," Ph.D. dissertation, University of Genoa and Italian Institute of Technology (IIT), Genoa, Italy, Apr. 2010.

[29] G. Fink, *Proprioceptive Sensor Dataset for Quadruped Robots*. IEEE Dataport, 2019, DOI:10.21227/4vxz-xw05.